Fabrication of tubular anti-resonant hollow core fibers: modelling, draw dynamics and process optimization

GREGORY T. JASION*, JOHN R. HAYES, NATALIE V. WHEELER, YONG CHEN, THOMAS D. BRADLEY, DAVID J. RICHARDSON, AND FRANCESCO POLETTI

Optoelectronics Research Centre, University of Southampton, Southampton, SO17 1BJ, UK
**g.jasion@soton.ac.uk*

Abstract: The fabrication of hollow core microstructured fibers is significantly more complex than solid fibers due to the necessity to control the hollow microstructure with high precision during the draw. We present the first model that can recreate tubular anti-resonant hollow core fiber draws, and accurately predict the draw parameters and geometry of the fiber. The model was validated against two different experimental fiber draws and very good agreement was found. We identify a dynamic within the draw process that can lead to a premature and irreversible contact between neighboring capillaries inside the hot zone, and describe mitigating strategies. We then use the model to explore the tolerance of the draw process to unavoidable structural variations within the preform, and to study feasibility and limiting phenomena of increasing the produced yield. We discover that the aspect ratio of the capillaries used in the preform has a direct effect on the uniformity of drawn fibers. Starting from high precision preforms the model predicts that it could be possible to draw 100 km of fiber from a single meter of preform.

OCIS codes: (060.0060) Fiber optics and optical communications; (060.2280) Fiber design and fabrication; (060.4005) Microstructured fibers; (000.4430) Numerical approximation and analysis.

1. Introduction

Hollow core microstructured fibers (HCF) guide light in an air core. Light confinement is provided by a precise geometric cladding which surrounds the core and is typically composed of air regions defined by silica membranes. Guiding light in a hollow core has dramatic advantages when compared to conventional all-solid fibers for many applications. In HCF light can travel at near vacuum speeds for ultimate low latency transmission [1], and non-linear effects can be reduced by 5 orders of magnitude due to the low interaction of light with the glass [2]. It is therefore possible to transmit extremely high optical power without damage [3], or to transmit wavelengths with lower loss than the bulk material, such as in the mid-IR or UV spectral regions in silica [4, 5]. Hollow core fiber can also be exploited for sensing applications, for example, a gas sample can be loaded into the core and optically interrogated over an extremely long interaction length, opening up the potential for a high sensitivity gas sensing device [6].

Fabrication of HCF follows a similar process to that used for conventional fibers: using a fiber drawing tower a preform (a macroscopic replica of the fiber to be drawn) – is lowered slowly into a vertical annular furnace where the glass softens and is drawn, under tension, down to fiber dimensions. Yet, during HCF draws control of the hollow regions of the structure adds additional complexity to the process. Practically, differential gas pressure is applied between different hollow regions in the preform (for example, between the core and cladding regions) in order to precisely control the fiber structure [7]. In most cases, the fibers are required to achieve considerably higher aspect ratios (ratio of inner to outer diameters) than the preforms they originate from. This necessitates the careful use of pressures to modify

the transverse structure as the preform passes through the hot zone. Controlling the process to achieve the desired structure can be extremely challenging. Real time optimization of the draw parameters during a fiber draw, in particular the applied gas pressure, is an expensive and time consuming activity, which is overly reliant on trial and error. Modelling of fiber draws is advantageous for both the increased efficiency of fiber drawing, i.e. choosing the correct parameters more quickly and wasting a smaller fraction of preform, and for the ability to explore the parameter space *a priori* in order to identify designs which are both feasible and provide high optical performance before performing expensive fabrication trials. Draw dynamics also need to be considered when designing the preform from which to draw these fibers. The geometric transition between preform and fiber that occurs within the draw furnace is non-trivial and is normally hidden from the fabricator [8-10].

Models of hollow microstructured fiber draws can be used to understand how the structure of the preform changes in the furnace and necks-down to fiber. Over the years fiber draw modelling has been approached in several different ways. Analytical models of the draw of basic capillaries allowed for the first examinations of the impact of gas pressure and surface tension [11]; these forces are key contributors to the dynamics of the internal microstructure. For more complex geometries a variety of approaches have been taken to account for the flow of glass with multiple internal free surfaces; finite element methods have been used but while mesh methods can be applied to any microstructure geometry, they typically require significant computational resources and long solution times [10]. Lagrangian methods have been employed to allow the mesh to move with the surfaces [12] which can offer improved resolution of the free surface but also require significant resources. Models based on tracking the boundary of the air-glass interface have been developed which do not require a full volumetric mesh [13-15]. These have demonstrated extremely good results for fibers with arrays of a small number of holes, but the assumptions of the method do not allow for slender glass membranes [15]. The only model to be successfully demonstrated so far for modelling the draw of HCFs with hundreds of high air-filing fraction holes and sub-wavelength sized membranes is the Microstructure Element Method (MSEM), a 2D Lagrangian method using linear fluid elements to make up the lattice [8]. Whilst the MSEM allows accurate reproduction of the drawing rheology of hollow core photonic bandgap fibers, which have a cladding formed by an array of several hundred nodes connected by a slender lattice of glass membranes, it struggles to model the draw of other families of HCFs in which the cladding is not a lattice of linear elements.

In this work, we develop a simple but very accurate model that can simulate the fabrication of tubular anti-resonant hollow core fibers. These fibers are formed by an array of thin capillary tubes only attached to the inner boundary of a tubular jacket [16]. We adapt the analytical capillary draw model developed by Fitt et al. [11] to find the evolution of the outer jacket tube; we then use this solution to calculate the evolution of the additional capillaries in the structure [17]. The model is validated by comparing its predictions with two different experimental draws, and used to explain the difference in their dynamics. Once validated, it is used to explore the impact of certain parameter choices when designing the geometry of a preform for maximum yield.

2. Tubular anti-resonant hollow core fibers

HCF can be split into two categories based on the guidance mechanism; photonic bandgap fibers confine light by surrounding the core with a periodic lattice of nodes, while anti-resonant fibers surround the core with a cladding of slender glass membranes of a specific thickness that are in anti-resonance with the core guided light. Hollow core anti-resonant fibers have many geometric variants defined by their cladding structure; these include (but are not limited to) Kagome and tubular designs. Whilst the first anti-resonant fibers with a Kagome lattice had attenuations of dB/m level, a significant improvement was achieved by imposing that their core shape possessed a hypocycloid (negative curvature) design [18, 19].

Despite the progress, Kagome designs are found to suffer intrinsically from the presence of glass junctions in their cladding structure that compromise their optical performance. At these junctions, the glass thickness is greater than in the connecting membranes, and therefore these parts of the geometry introduce resonances that increase the loss of the fiber at multiple spectral locations within the transmission window. To eliminate the problem of connecting membranes, non-contacting tubular geometries such as that shown in Fig. 1 have received much attention in recent years due to the simplicity of both design and fabrication approach. Since the cladding membrane thicknesses are uniform and there are no nodes or glass junctions, these fibers can provide broad and smooth transmission windows and have rapidly become very attractive for numerous applications [16, 20, 21]. The tubular geometry has also paved the way for a new generation of hollow core fibers with one or more membranes aligned azimuthally. These new anti-resonant fibers have the potential to challenge conventional fibers in many applications [22-25]. In this paper, we focus on simulating the drawing process of tubular anti-resonant HCF. More advanced nested geometries such as the nested antiresonant fiber (NANF) can be derived from this approach and will be the focus of future work.

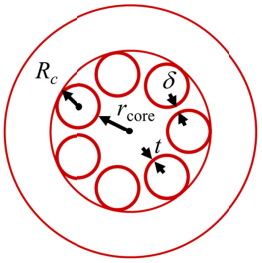

Fig. 1. An example of a 7 capillary tubular HCF geometry and its parameters: core radius, r_{core}, capillary thickness, t, capillary radius, R_c, and gap size, δ.

The primary loss mechanism in tubular HCFs is confinement or leakage loss, which is governed by the geometry. This is a function of core size and distance between core boundary and outer jacket, which in turns depends on the number of capillaries surrounding the core and on the size of the gaps between capillaries, Fig. 1. Since all of these geometric features are coupled, when a fiber is drawn all design requirements must be met simultaneously. For example, if a fiber is made with capillaries that are smaller than intended, for mass conservation they will also be too thick and as a result the low loss window will be shifted to longer wavelengths, while the core size and the gaps will be too large. Confinement loss can be reduced by having large capillaries with the small gaps between neighbors [23, 26], typically 1-3 wavelengths. If the gaps are too large, light will leak through them and the confinement loss will also be large; if the gap vanishes and the tubes are in contact a thicker node of glass is created which will obscure the transmission window with resonances. For reduced bending losses it is known that having a large number of smaller capillaries is better as it reduces interactions between capillary (cladding) modes and core guided modes [27] but even in this case the gaps need to be carefully controlled. In summary, the ultimate challenge in the draw of tubular fibers is controlling the size of the capillaries to achieve the specified core radius, capillary thickness and gap size, while avoiding contact.

Sections 3 and 4 will introduce our model and its experimental validation. The latter sections of this work will then use the model to explain the challenge of controlling the gap size. As will be shown, the capillaries do not respond linearly to pressure, making it difficult to predict the required pressures for a given design. The model is also able to reveal mid-draw dynamics, hidden to the fabricator, which can severely limit the achievable gap size in the final fiber. It will be shown that the model can be used to predict pressure values with good accuracy, foresee when draw dynamics become prohibitive, and help design preforms to avoid it.

3. The model

The draw model is designed to accurately represent a physical fiber draw with many of the same inputs and control parameters, and therefore we will first describe the experimental process. HCFs are typically made using a two stage stack and draw process [28]. In the first stage, a preform is assembled by stacking capillaries and spacing elements into a slender jacketing tube, 20 – 30 mm in outer diameter, this preform is subsequently drawn into canes, Fig. 2(a), which are a few millimeters in diameter. Next, a cane is inserted inside a substantially thicker jacket tube, ~10 – 30 mm in outer diameter, to construct the second stage preform. This is drawn to fiber, Fig. 2(b), using a fiber drawing tower, Fig. 2(c). During the fiber draw, an inert gas is applied to two regions, each with independent pressure control: the core and the tubular capillary elements. The gas pressure is applied to counteract the effect of surface tension and to control the geometry; this will be discussed in detail in the next section. The primary inputs available to fabricators are the feed and draw speeds, the temperature of the furnace and the core and capillary gas pressures. To first approximation, these are responsible for: the fiber diameter, the draw tension, the diameter of the hollow cladding, and the diameter of the capillaries respectively. However, as we will show below, many of these outputs are coupled in more subtle ways.

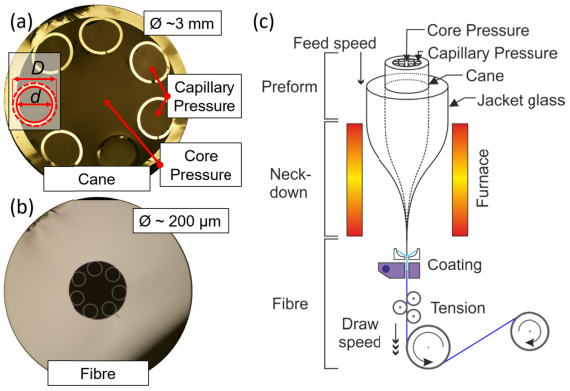

Fig. 2. (a) The 2nd stage preform (cane), (b) the fiber, (c) diagram of the fiber drawing process.

As we have discussed, there are several approaches to modelling the draw of optical fibers. Since these fibers are based on tube like structures we propose a method which is an extension of the simple analytical model for the draw-down of single tubes, known as the Fitt model [11]. Our model solves the original Fitt equations for the jacket tube to find the geometric transformation of the tube through the neck-down in the furnace, from preform down to the final fiber dimension. To calculate the drawdown of the inner capillaries that make up the microstructure we use the axial part of the jacket tube solution, while the lateral dynamics (expansion or contraction) of each capillary are solved uniquely. This follows from the physical interpretation that since the elements in the microstructure are bonded to the jacket, the jacket carries the vast majority of the draw tension, and the capillaries' extensional deformation is determined by the evolution of the jacket. The lateral dynamics of the cladding capillaries are solved separately and determined by their individual geometry, gas pressure, surface tension and viscous stress in the glass.

The shape of the neck-down of the jacket tube is found by solving:

$$\rho\left(R_j^2 - r_j^2\right)\left(w\frac{\mathrm{d}w}{\mathrm{d}z} - g\right) = \frac{\mathrm{d}}{\mathrm{d}z}\left(3\mu\left(R_j^2 - r_j^2\right)\frac{\mathrm{d}w}{\mathrm{d}z} + \gamma\left(R_j + r_j\right)\right) \tag{1}$$

$$\frac{\mathrm{d}}{\mathrm{d}z}\left(r_j^2 w\right) = \frac{\mathrm{d}}{\mathrm{d}z}\left(R_j^2 w\right) = \frac{p_{\mathrm{core}} r_j^2 R_j^2 - \gamma r_j R_j\left(r_j + R_j\right)}{\mu\left(R_j^2 - r_j^2\right)} \tag{2}$$

$$\frac{R_j^2 - r_j^2}{2}\left(\rho c_p w \frac{dT}{dz} - \sigma\alpha\left(T_a^4 - T^4\right)\right) = R_j N\left(T_a - T\right) \tag{3}$$

where the inner and outer radii, $r_j(z)$ and $R_j(z)$, and the speed, $w(z)$, are a function of the axial position, z, resulting in the fiber dimensions at a position $z = L$ after the glass has cooled and all changes have ceased, Fig. 3. The temperature of the glass is given by T; p_{core} is the gas pressure applied inside the core and g is the acceleration due to gravity; the density and surface tension of fused silica, the material in this work, are given by ρ=2200 kg/m^3 and γ=0.3 N/m. The thermal properties of specific heat and Stefan-Boltzmann constant are given by c_p=1345 J/kgK, σ=5.67x10^{-8} W/m^{2}K^4 respectively; while α=0.885 1/m, is a material property involving emissivity and N=100 W/m^{2}K is a heat transfer coefficient, all assumed to be temperature invariant. The furnace temperature is given by $T_a(z)$.

The Fitt model uses a simple heat transfer approach, Eq. (3). While many more complex approaches have been used in other works [29], we found that trying to accurately recreate the temperature distribution or thermal parameters, such as N or α, is unnecessary, and accurate results can be obtained by simply matching the draw tension between experiment and simulation [30]; similar conclusions have been reached by others, for example in [9, 31]. Nevertheless, a furnace profile must be defined to solve the equations, in this work it is defined as Gaussian curve with peak temperature, $T_{a,\max}$, chosen to achieve a target tension, the position of the peak temperature, $z_{a,\max}$ = 0.04 m, standard deviation, σ_a = 0.06 m, furnace length, L_a = 0.065 m, after which $T_a(z>L_a)$ = 293 K. The computational domain, L, is chosen to be long enough that the viscosity reaches such high values that all geometric changes are halted – akin to the fiber being sufficiently cool. While at the inlet, the preform temperature at z = 0 is chosen to be 500 K cooler than the furnace temperature, these are found to give smooth neck-profiles without discontinuities. An example of furnace and neck-down temperature is given in Fig. 3 with $T_{a,\max}$ = 1825 °C.

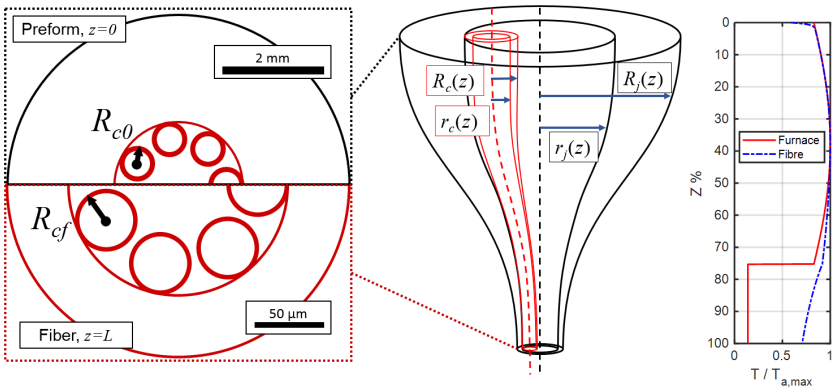

Fig. 3. Schematic of preform, fiber and neck-down with nomenclature and an example of a furnace and fiber temperature profile.

Equations (1)-(3) have been simplified from the original expressions provided in [11] to remove the temporal terms. We also chose to remove the term related to heat conduction which is known to be small in silica glass. The viscosity of glass, μ, is given by the fitted function of Urbain [32], given in [33], for glass temperatures between 1400 and 2500 °C where our process operates, viscosity has units of Ns/m^2 and temperature has units of K,

$$\mu = 5.8\times10^{-8}\exp\left(\tfrac{515400}{8.314T}\right) \tag{4}$$

The differential system, Eqs. (1)-(3), is solved to find the fiber inner and outer radius by marching through the neck-down in z. The boundary conditions are that all geometric values are known at z = 0, given by the preform geometry, and likewise the initial feed rate, $w(0)$. The pressure is assumed constant throughout z. This is an initial value problem in which a

goal seek algorithm is used to find the value of dw/dz at $z = 0$ for a target outer fiber radius, $R_{jf} = R_j(L)$, p_{core} can be found in a similar way for a target inner fiber radius or directly specified. We use a second order Runge-Kutta scheme. With $\Delta z = r_j \times 10^{-4}$, the ratio of input and output volume fluxes shows a discrepancy of less than 1×10^{-4}; this is proportional to the step size and can be reduced further if desired at the cost of increased solution time.

The fiber draw tension is experimentally measured some distance below the furnace (Fig. 2); numerically, to first order approximation, it can be determined at any point by:

$$\tau = 3\mu \frac{\mathrm{d}w}{\mathrm{d}z} \pi \left(R_j^2 - r_j^2 \right) \tag{5}$$

Tension is directly proportional to the viscosity of the glass which regulates the dynamics between pressure and surface tension, Eq. (2). The viscosity itself reduces with increasing glass temperature, Eq. (4). The glass temperature is controlled by the furnace temperature, Eq. (3), which along with the pressures, feed and draw speed, is one of the inputs available to the fabricator. In the model, after the neck-down of the jacket tube has been solved the draw tension is determined; to simulate a fiber draw with specific tension, the peak furnace temperature can be modified and the system solved again.

In the remainder of this work, we will present results of experimental and simulated fiber draws with a variety of preform geometries. To simplify matters we will define some explicit nomenclature. As previously introduced, subscript c denotes a capillary parameter, and j a jacket tube parameter, while an additional subscript of 0 denotes a preform parameter (at $z = 0$) and f a fiber quantity ($z = L$). The capillaries in the cane preform have an inner and outer diameter of $\mathrm{d}_{c0} = 2r_c(0)$ and $D_{c0} = 2R_c(0)$, respectively, while the internal capillaries of the fiber geometry are given by $d_{cf} = 2r_c(L)$ and $D_{cf} = 2R_c(L)$. The fiber inner and outer diameter is defined as d_{jf} and D_{jf}, and the thickness of the capillaries of the fiber are defined as $t_{cf} = R_{cf} - r_{cf}$.

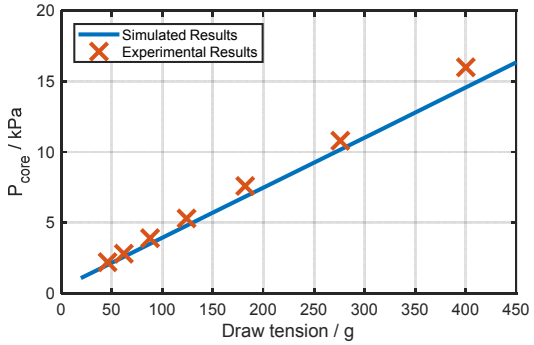

Fig. 4. Capillary draw with constant d_f/D_f, pressure required at different draw tensions.
Experimental Capillary draw, crosses, compared with results found from Fitt model, solid line.

To validate this jacket tube draw model we performed a simple experiment; we drew a Heraeus F300 fused silica glass jacket tube [34] with an outer diameter of D_{j0} = 9.96±0.05 mm and inner diameter of d_{j0} = 3.43±0.05 mm down to fiber dimensions with outer diameter, D_{jf} = 180 µm, and inner diameter, d_{jf} = 90 µm. The preform feed speed was 3 mm/min. We drew the capillary at 7 different tension values by modifying the furnace peak temperature, and recorded the internal pressure, p_{core}, that allowed us to maintain a 50% expansion ratio (ratio of inner to outer diameters) in the final fiber. This experiment was simulated by solving the system of Eqs. (1)-(3), the simulated furnace temperature and core pressure were modified to match the draw tension and expansion ratio in each case. Figure 4 shows the comparison of the simulation and the experimental data points: it is clear that the model matches the experiment very well. Increasing the draw tension increases the glass viscosity, which in turn increases the required pressure to cause a relative expansion of the tube. This intuitive

behavior can be seen in Eq. (2) in which the viscosity (proportional to draw tension, Eq. (5)) is in the right hand side denominator, while the pressure is in the numerator. The model appears to be consistently underestimating the pressure required by about 5%; this could be caused by a drop in pressure due to gas flow in the narrow capillary, or alternatively the tension could be overestimated due to the additional drag of applying the coating [35].

To extend the model to tubular HCF we added additional capillaries to the model, inside the jacket, Fig. 3. To do that, we made the assumption that all the axial terms found for the jacket tube solution apply equally to the internal capillary tubes. Since we now have a solution for $w(z)$, we can simply take Eq. (2) and substitute r_j and R_j for the inner and outer radius of the internal capillary, r_c and R_c, which are both known at $z = 0$. The core pressure is substituted for the applied pressure difference, $\Delta p = p_{\text{capillary}} - p_{\text{core}}$ which is the difference between the core pressure seen by the jacket tube and the pressure applied inside the capillary. We also use the glass viscosity profile, $\mu(z)$, from the jacket tube solution along with all the same material properties. For clarity, this expression has been rearranged with the physically relevant grouping on the right hand side, respectively: pressure, surface tension, and viscosity in the denominator:

$$\frac{\mathrm{d}}{\mathrm{d}z}\left(r_c^2 w\right) = \frac{\mathrm{d}}{\mathrm{d}z}\left(R_c^2 w\right) = \left[\Delta p - \gamma\left(\frac{1}{r_c} + \frac{1}{R_c}\right)\right]\frac{r_c^2 R_c^2}{\mu\left(R_c^2 - r_c^2\right)} \tag{6}$$

In summary, the steps to be followed to model a tubular anti-resonant hollow core fiber draw are as follows:

1. Define the preform geometry, the targeted draw tension, and the target fiber outer and inner radii.
2. Make an initial estimate of $\mathrm{d}w/\mathrm{d}z$ at $z = 0$ and solve Eqs. (1)-(3) by marching in z.
3. Using a goal seeking algorithm find $\mathrm{d}w/\mathrm{d}z$ at $z = 0$ and p_{core}, which satisfy the target fiber outer and inner radii, respectively.
4. Modify the peak furnace temperature to achieve the target draw tension, then perform step 2 and 3 again. Once the tension is matched the jacket glass solution is complete.
5. Solve Eq. (6) for the internal capillaries by marching in z using $w(z)$ and $\mu(z)$ from the solution of step 2.

Mid-draw contact

When additional capillaries are included in the structure some interesting dynamics emerge. As mentioned previously, drawing a tube down to fiber requires internal gas pressure without which the surface tension would cause the central hole to reduce and potentially collapse completely. Surface tension produces a pressure proportional to the inverse of the radius of curvature, $p_\gamma = \gamma / r$. As the internal capillaries are smaller than the jacket, the surface tension acting on them will be larger and therefore a higher pressure is required to prevent collapse of the capillaries than for the jacket, and as such Δp should always be positive. However, the dimensions of the geometry reduce as the preform is drawn to fiber. This leads to a dynamic that was first described in modelling work on hollow core photonic band gap fibers [8] but applies to all hollow fiber draws with applied pressure regions. In the first part of the draw-down the geometry is larger, the pressure dominates and the capillaries expand. In the latter half of the draw-down, the geometry is smaller and now surface tension dominates: the capillaries will start to contract until the glass is cool and the high viscosity prevents change. This relationship can be seen on the right hand side of Eq. (6) where the pressure term, Δp, is positive, while the surface tension term, $\gamma(1/r_c + 1/R_c)$, is negative. If parameters are chosen correctly, the targeted fiber geometry can be obtained at the end of this dynamic process. This process, however, requires the capillaries to somewhat overshoot their targeted relative dimension in the expansion phase, to pre-compensate for the subsequent contraction phase. The fiber draw tension, Eq. (5), is linearly proportional to viscosity which appears in the denominator of Eq. (6) and as such will regulate this dynamic; a high draw tension will reduce

the effect of both pressure and surface tension and the extent of any expansion or contraction and therefore reduce any overshoot required.

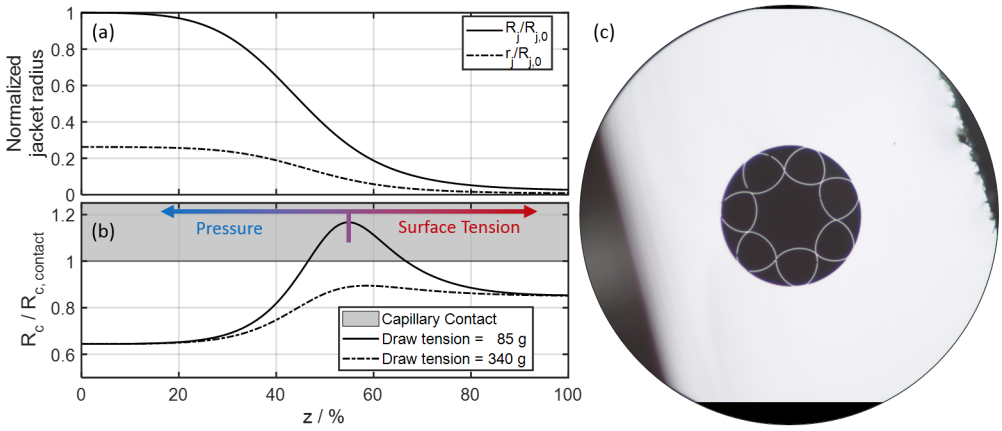

Fig. 5. Mid-draw contact occurs as a possible consequence of the expansion and contraction phases of the capillaries during the neck-down. (a) The normalized outer and inner radius of the fiber jacket through the neck-down. (b) The radius of the internal capillaries during neck-down for a high and low tension case normalized to the radius at which contact occurs, the regions where surface tension or pressure dominate are indicated. (c) An experimental example of a fiber that has contacted mid-draw showing evidence of contraction after contact. Visualization 1 shows how the simulated structures change through the neck-down.

For a simple capillary draw, this observation is somewhat inconsequential, however, if we are examining the behavior of capillaries that form the cladding part of a hollow core tubular fiber, then they have a limited amount of space for expansion, and these dynamics become very significant. To illustrate this behavior, draw simulations of a 7 capillary fiber were performed at 2 draw tensions. The neck-down of the jacket tube is shown in Fig. 5(a) as a function of z, while Fig. 5(b) shows the capillary radius through the neck-down for two different draw tensions, normalized to the size at which contact occurs between neighbors: $r_{c,\mathrm{contact}} = r_j \sin(\pi/n)/(1+\sin(\pi/n))$, where n is the number of capillaries, for a 7 capillary fiber this is $r_{c,\mathrm{contact}} \sim 0.3\, r_j$. The peak of the relative capillary size in Fig. 5(b) indicates the position in the neck-down where the transition from pressure to surface tension dominated change occurs, this can be found from Eq. (6). For both tensions, Δp was chosen to target the same capillary size in the fiber at the end of the neck-down. As predicted, the higher draw tension shows a modest contraction and only requires a moderate overshoot. In contrast, the lower draw tension has a very aggressive contraction phase and requires so much pre-compensation pressure that the capillaries would join with their neighbors resulting in mid-draw contact. Alternatively, a lower pressure could be used to avoid contact but the result would be smaller capillaries than intended in the final fiber.

Contact, if it occurs, will happen in the middle of the draw-down near the hottest part of the glass. Once the neighboring capillaries have come into contact, they fuse together and will not separate in later stages of the draw, despite the work of surface tension. The geometry is therefore compromised. A structure that has experienced mid-draw contact will still present morphology from the contraction phase in the latter half of the draw: the internal capillaries will tend towards a triangular shape due to the dominance of surface tension. An experimental example is shown in Fig. 5(c). Mid-draw contact needs to be avoided, but for good optical performance the inter-capillary gap needs to be as small as possible. The smallest achievable gap is related to the amount of contraction induced by surface tension experienced by the capillaries, and must be considered when planning a new preform.

4. Experimental validation: tubular anti-resonant hollow core fiber

In this section we compare our model with two different experimental HCFs: a 6 capillary (6C), and a 7 capillary (7C) fiber. These fiber geometries were designed to have capillary thicknesses of approximately 370 nm and 700 nm respectively, and to minimize their leakage loss we aimed to keep the gap between neighboring capillaries small, while avoiding any mid-draw contact. Table 1 summarizes the preform geometry and draw parameters for the two draws.

Table 1. Preform geometry and draw parameters for experimental validation.

	Fiber		
	6C	7C	
Cane capillary diameter ratio: d_{c0}/D_{c0}	0.67	0.82	
Cane capillary diameter: D_{c0}	440	480	µm
Cane diameter	2.9	2.4	mm
Jacket tube: d_{j0}/D_{j0}	3 / 10	2.7 / 9.4	mm
Fiber diameter: d_{jf}/D_{jf}	100 / 220	80 / 255	µm
Fiber capillary thickness: t_{cf}	370	700	nm
Draw tension: τ	300	340	g
Draw stress	98	72	MPa
Fiber yield / 1m of preform	2.4	1.4	km/m

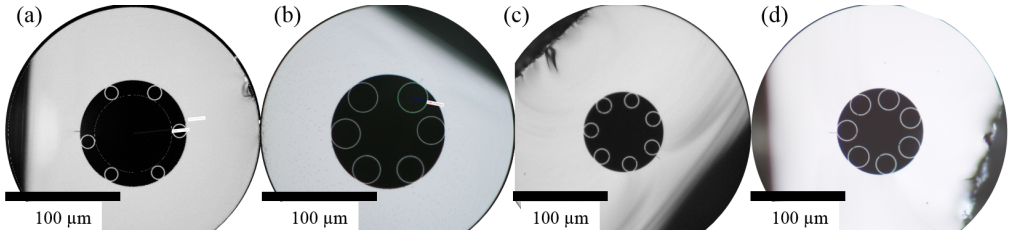

Fig. 6. 6C fibers with low, (a), and high, (b), capillary pressure. 7C fibers with low, (c), and high, (d), capillary pressure.

During each fiber draw several samples were taken with increasing capillary pressure applied to expand the capillaries while keeping the core pressure fixed to maintain the same overall fiber dimensions. Experimental images of both fibers with low and high capillary pressure can be seen in Fig. 6(a-d). The simulations used the same geometric and draw parameters as the experiment, and furnace conditions were chosen to match the experimental fiber draw tension.

The capillary diameters of each fiber sample were measured and their mean value is plotted in Fig. 7. The error bars indicate the minimum and maximum diameters measured across all the capillaries; the solid lines show the simulated capillary diameter versus delta pressure. To correctly predict the pressure required by the capillaries they must be accurately measured at the preform stage otherwise a constant offset in pressure between simulation and experiment is observed. But since the pressure offset is constant, the model can be calibrated with an initial data point. Figure 7 shows an excellent agreement between the model and the experimental results, and also illustrates the differences in the dynamics between the two cases. Both cases show the non-linear response of the capillary diameters to the applied pressure. This is because increasing the pressure will make the tubes larger but also thinner, and thinner tubes have less viscous resistance to change, Eq. (6). The 6C, Fig. 7(a), needs larger delta pressure because the capillaries in the cane are thicker than the 7C, but the 7C, Fig. 7(b), has a shallower gradient than 6C because there is less relative transformation

between the aspect ratios of the cane capillaries and the fiber ones. This notion of an amount of transformation is best quantified by the fiber yield: Table 1, provides this in units of km/m of preform. The target geometry is near the maximum diameter indicated in Fig. 7, but as the slope of the diameter versus pressure curve is increasing, it makes it difficult to estimate the exact pressure required to achieve the target. Achieving the target in the 7C case was therefore much easier than the 6C.

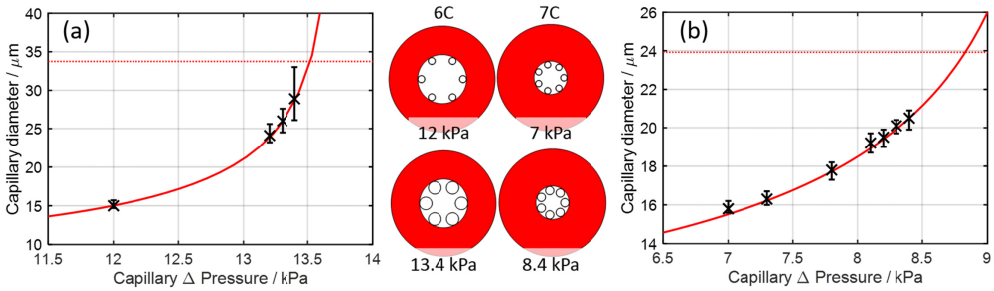

Fig. 7. Comparison of the simulated results and mean of the measured capillaries in the 6C fiber (a), and the 7C fiber (b). The error bars indicate the range of measured values; the diameter when the capillaries touch is indicated as the dotted horizontal line. Simulated fiber geometries are shown at the specified pressures.

We have now demonstrated that the model can be used to adequately predict the draw parameters and pressures required to achieve a specific geometry. This capability can be used to reduce experimental trial and error and to increase fabrication efficiency by allowing fabricators to reach the targeted geometry in a fewer number of steps. Now that the model has been validated against a pair of experimental cases we will use it to explore the structural variations amongst capillaries already evident in the error bars of Fig. 7. Following that, we will apply it to the task of designing fiber preforms for greatly increased fiber yields.

5. Propagation of structural variations from preform to fiber

Cross-sectional uniformity in the final fiber is extremely important. From mass conservation, the thickness and diameter of the capillaries surrounding the core are related; variations in thickness will broaden the resonances and erode the low-loss window bandwidth, while irregular capillary diameters lead to larger gaps between capillaries which contribute to increased leakage loss. As such, it is important to identify the sources of non-uniformity and to understand how they can be mitigated through design.

The experimental data in Fig. 7 showed how the capillaries responded to pressure. The range of capillary sizes across the fiber structure as given by the error bars in Fig. 7 and showed a dramatic difference between the two fibers. It is clear that the 6C case showed a much larger range of capillary sizes than the 7C case. It is reasonable to assume that the temperature and pressure are applied uniformly across the geometry as the heating process is radiative and there are no substantial gas flows in the pressurization system. However, the capillary tubes in the preform may have some small variation amongst them. For the stack and draw technique these inner capillaries will typically have been fabricated in-house from a single tube and non-uniformities in this starting tube or some small drift in conditions during the fabrication would result in some small differences among the capillaries. If there are subtle differences in the initial preform geometry how do they propagate into the drawn fiber?

To explore this idea, we used the model of Section 3 to virtually ‘draw’ a fiber with a range of subtly different capillary tube sizes in the cane, at a single pressure. For the 6C case we examined the experimental result at 13.4 kPa which resulted in fiber capillary diameters ranging from D_{cf} = 26 to 33 µm. The cane capillaries were modelled with a fixed cross sectional area and a range of D_{c0} = 442 to 446 µm. Figure 8(a) shows the simulated fiber capillary diameters for this range of preform diameters. A few measured fiber capillaries are

shown in red, and the intersection with the simulated curve yields the expected cane capillary diameters from which they would derive. The model shows that for the 6C case a ~0.5% variation in the preform is enough to provide ~20% variation in the final fiber. Expressed in terms of sensitivity, the change of fiber capillary diameter with cane capillary diameter was found to be 2.9 µm / µm. The identified range of preform dimensions was virtually drawn across the range of pressures to compare with the experimental range of capillary diameters at all data points, Fig. 8(b), showing good agreement with the upper and lower bounds across the dataset.

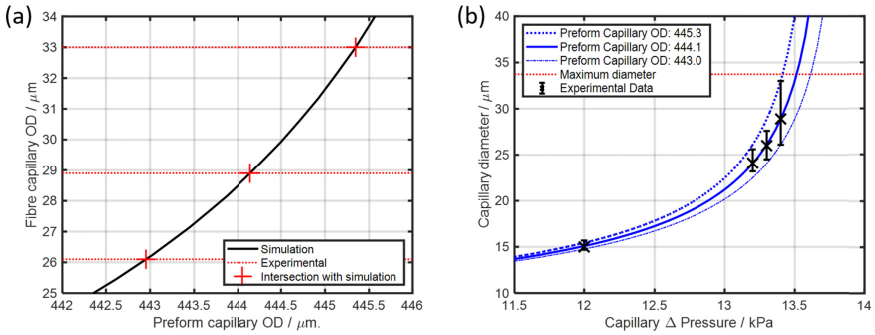

Fig. 8. A cane with a range of subtly different capillaries was drawn to fiber. (a) The final capillary size when all the cane capillaries were drawn at the same pressure, the intersection of the experimental values suggests the expected range of cane capillary diameters in the experimental case. (b) Full range of pressures applied to a cane with the identified range of capillary pressures, plotted with the experimental results.

Examining Fig. 7, the question arises as to why the 7C case shows a smaller variability among the experimental capillaries as compared to the 6C case. Two factors contribute directly: the 6C case had smaller d_{c0}/D_{c0} (thicker) cane capillaries that needed more expansion, and thinner capillaries in the final fiber, which are more sensitive to changes. To test this hypothesis, we modified the 6C cane capillary dimensions to have the same d_{c0}/D_{c0} as the 7C case, and targeting the same fiber geometry (while conserving the cross-sectional area and with it the yield). We then introduced variations in the cane capillaries and virtually drew it to fiber. The resulting fiber capillary diameter to cane capillary diameter sensitivity was then reduced to only 1.2 µm / µm, less than half the original sensitivity. This demonstrates that the increasing the d_{c0}/D_{c0} of the cane capillaries makes the fiber less sensitive to variation introduced in the preform fabrication process and it is therefore clearly advantageous.

This section discussed structural variation that was constant along the length and therefore steady in time. It is worth commenting that variations in process conditions which fluctuate with time will have a complex influence on the produced fiber. For example, a sudden change in pressure will be felt simultaneously throughout the neck-down. The fiber produced after this event will not be uniform as each part of the neck-down will have a unique history. These transient dynamics will be explored in future work.

6. Increasing the yield

All of the tubular experimental fibers presented to date have been fabricated at research-scale facilities and from small preforms, with successful bands of fiber only a few hundred meters in length. For comparison, the longest reported hollow core fiber of any kind was a photonic band gap fiber of 11km in length [36]. As mentioned above, designs related to the tubular fiber geometry are extremely promising for a range of applications, which creates a demand for the yield and production rate of these fibers to be increased for commercial uptake and cost reduction purposes. To this end, we have used our model to investigate the feasibility of drawing up to 100km of fiber from a single meter of preform. In order to do this we had to consider some additional design decisions. Designing microstructured fiber geometries has

been the subject of many previous works [23, 37-43] , but designing the preforms from which to draw these fibers has received considerably less attention. For tubular fibers, the tubes that make up the preform can be small and thick or large and thin whilst having the same volume of glass and leading to the same final fiber geometry. Changing this single parameter can have vastly different outcomes in terms of pressure parameters, sensitivity to preform variation, and mid-draw contact. In the following we investigate the trade-offs.

We designed six different preforms with nominal yield ranging from 1 to 100km of fiber per meter of preform, shown in Table 2, all targeting the same fiber design, presented in Table 3. For each targeted yield we simulated 4 preforms with d_{c0}/D_{c0} from 0.2 → 0.8, creating 24 cases in total, and we modified D_{c0} to maintain the same glass area in the cane. The combined glass of both the cane sleeve and the jacket tube (d_{j0}/D_{j0}) was chosen to be 0.33 in all cases, the same value as in the fiber design. The impact of modifying this parameter was found to be minimal and will not presented here. For each of these simulated draws the draw tension was set to 400 g. As previously mentioned, a higher draw tension allows for better control of the geometry, but a too high tension risks breaking the fiber.

Table 2. Second stage preform dimensions for the yield upscaling study, all preforms produce the fiber geometry defined in Table 3. The experimental 7C preform is marked with an asterisk and its fiber dimensions are given in Table 1.

Yield, Y	Jacket glass		Cane Capillary	
km / m	D_{j0} / mm	d_{j0}/D_{j0}	D_{c0} / mm	d_{c0}/D_{c0}
1.0	6.3	0.33	0.20 → 0.33	0.2 → 0.80
*1.4**	*9.4*	*0.29*	*0.480*	*0.82*
5.0	14.1	0.33	0.46 → 0.73	0.2 → 0.80
10.0	20.0	0.33	0.64 → 1.04	0.2 → 0.80
25.0	31.6	0.33	1.00 → 1.64	0.2 → 0.80
50.0	44.7	0.33	1.42 → 2.32	0.2 → 0.80
100.0	63.2	0.33	2.00 → 3.28	0.2 → 0.80

Table 3. Target fiber geometry for yield upscaling study.

D_{jf}	200	µm
d_{jf} / D_{jf}	0.33	
Core diameter	30	µm
Capillary, D_{cf}	18.1	µm
Capillary thickness, t_{cf}	550	nm
Draw Tension, τ	400	g

Increasing the yield of the draw means increasing the ratio of lengths of fiber produced to preform consumed. In turn this requires an increase in the strain rate, dw/dz. From Eq. (5) in order to maintain a constant draw tension, the viscosity must be reduced which can be achieved by increasing the furnace temperature. However, this has the undesired impact of decreasing the transverse stiffness of the microstructure, making it more sensitive to applied pressure changes, and rendering fine control of the gap between capillaries more challenging.

For each case, we calculated the additional pressure that is required inside the capillaries, Δp, in order to achieve the target fiber capillary size. Figure 9(a) shows the capillary pressure for each case. Its relationship with the yield Y was found to be approximately $\Delta p \propto Y^{-0.8}$, with the smaller d_{c0}/D_{c0} cases requiring more pressure than the high ones. This is to be expected from Eq. (5) given the increase in viscous stress. Interestingly, the sensitivity of the final capillary diameter to the applied pressure, Fig. 9(b), was found to be almost invariant with

d_{c0}/D_{c0} at shorter yields, and with a power relationship with yield of approximately $dD_{cf}/d\Delta p \propto Y^{1.5}$. This dramatic increase of the sensitivity to pressure for the longest yields would require in practice very precise and very stable pressure controllers, able to impose differential pressures of only fractions of a Pa. The pressurization system would also need to be engineered such that all capillaries see the same pressure, with the tolerated pressure variations becoming increasingly smaller as the yield increases.

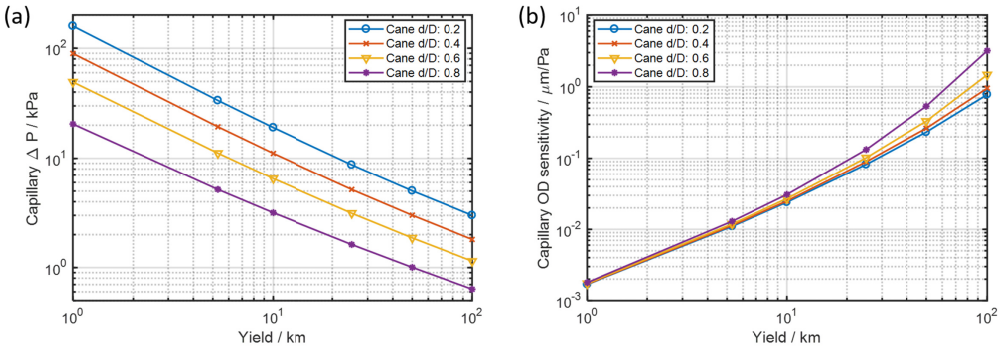

Fig. 9. (a) Capillary pressure required, comparing larger yield preforms with different d_{c0}/D_{c0}. (b) Sensitivity to pressure for larger yield preforms.

The 7C experimental case discussed above has slightly different dimensions and a yield of 1.4 km/m, but shows a sensitivity of 6 nm/Pa similar to the 3 nm/Pa result expected for ~km/m yield in this study. For the 10 km yield case, this increases to ~20 nm/Pa. In practice, to achieve a capillary diameter of 18.1 ± 0.5 µm in the 10 km case, the pressure would need to be controlled to within ± 0.25 kPa, while the absolute value chosen is between 3 and 20 kPa depending on the d_{c0}/D_{c0}.

The reduction of the required pressure and the increased sensitivity at longer yields is due to a combination of an increased cane geometry size, which shifts the relationship between pressure and surface tension, and a reduction in viscosity in the glass that is required to maintain the draw tension at 400g [30].

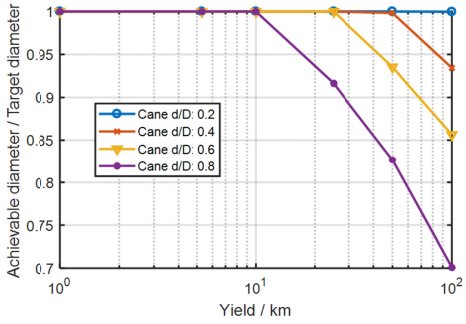

Fig. 10. The impact of mid-draw contact is shown by plotting the achievable capillary diameter that can be drawn before mid-draw contact occurs, normalized to the target capillary diameter as a function of preform yield.

In all cases, pressure was applied to achieve a fiber capillary diameter of d_{fc} =18.1 µm. As the yield increased, mid-draw contact was found to occur more easily. To illustrate this, the largest capillary diameter that could be drawn without mid-draw contact was identified for each yield and for each d_{c0}/D_{c0}. The results are summarized in Fig. 10, normalized to the target capillary diameter of 18.1 µm: a value of 1 indicates that the target fiber capillary diameter was achieved. It can be seen that reducing the d_{c0}/D_{c0} to 0.2 is essential to avoid contact for the 100km yield fiber, while a preform with d_{c0}/D_{c0} = 0.8 would be limited to

about 10km as beyond that it would either suffer from mid-draw contact or from smaller than desired capillaries. The study in the previous section recommended increasing the d_{c0}/D_{c0} (thin initial tubes) to avoid amplifying the structural variations among the capillaries in the preform. In this section however, a low d_{c0}/D_{c0} has been shown to help avoid mid-draw contact when aiming to increase the yield of these preforms. Given these findings, we conclude that in order to unlock the capacity for greater yield, emphasis must point towards increasing the uniformity of the canes produced, which will need to have relatively thick capillaries to avoid mid-draw contact.

7. Conclusions

A virtual draw model for the prediction and understanding of the fabrication of tubular anti-resonant hollow core fibers has been developed and validated. The model has been developed to assist the fabrication of these fiber types and provide information to help tailor the size of the internal capillary tubes and the gaps between them. The model solves a jacket tube neck-down first, and it uses the axial solution found for this case to calculate the lateral dynamics of the internal tubes. The model was validated with two different experimental draws, showing a remarkable agreement. This demonstrates that such a model can be an effective tool for predicting the draw parameters required, in particular the pressure needed by the internal capillaries to achieve a given target. Experimental fiber draws are generally a black box, with only the input parameters (preform and draw inputs) and the output structure (fiber) directly measurable during the draw. The preform dynamics in the neck-down within the furnace are normally hidden. Using the proposed model we have analyzed these dynamics, controlled by a competition between pressure and surface tension, and found that the first half of the neck-down is dominated by pressure, leading to an expansion of the internal capillaries, while in the latter half surface tension leads to their contraction. These dynamics can cause mid-draw contact between capillaries in the structure, which is irreversible and compromises the outcome of the draw. Having identified this dynamic, we then used the model to explore the main free design parameter, the preform capillary aspect ratio (d_{c0}/D_{c0}), for two case studies: the propagation of structural imperfections from the preform to the fiber, and the draw of preforms with increased yield. It was found that structural variations in the preform were mitigated by using large values of d_{c0}/D_{c0}, while mid-draw contact was best avoided by using small d_{c0}/D_{c0}. Our study indicates that to enable the draw of ~100 km scale lengths from a single preform significant engineering effort will need to be placed on the reduction of preform asymmetries and in ways to very accurately control pressures during the draw.

This model has been demonstrated to be an effective tool for predicting parameters and geometries for fiber draws. If used correctly, it can dramatically increase the fiber fabrication productivity, especially in a research environment where different structures are frequently drawn and draw parameters are often unknown. The fibers explored in this work operate in the near IR, but the model is equally capable of assisting the draw of geometries with thicker struts for mid-IR transmission or of geometries with much thinner capillaries for the visible or UV wavelengths. There is also no restriction on the type of glass used – borosilicate or chalcogenide glass could be easily substituted, even polymers could be included with appropriate consideration of the material properties.

All data supporting this study are openly available from the University of Southampton repository at https://doi.org/10.5258/SOTON/D0894.

Funding

Royal Academy of Engineering research fellowship; Royal Society university research fellowship; European Research Council program LightPipe (682724); and UK Engineering and Physical Sciences Research Council (EP/N00762X/1, EP/P030181/1).

References

1. F. Poletti, N. V. Wheeler, M. N. Petrovich, N. K. Baddela, E. Numkam Fokoua, J. R. Hayes, D. R. Gray, Z. Li, R. Slavik, and D. J. Richardson, "Towards high-capacity fibre-optic communications at the speed of light in vacuum," Nat. Photonics **7**, 279-284 (2013).
2. B. Debord, M. Alharbi, L. Vincetti, A. Husakou, C. Fourcade-Dutin, C. Hoenninger, E. Mottay, F. Gérôme, and F. Benabid, "Multi-meter fiber-delivery and pulse self-compression of milli-joule femtosecond laser and fiber-aided laser-micromachining," Opt. Express **22**, 10735-10746 (2014).
3. S. A. Mousavi, H. C. H. Mulvad, N. V. Wheeler, P. Horak, J. Hayes, Y. Chen, T. D. Bradley, S.-u. Alam, S. R. Sandoghchi, and E. N. Fokoua, "Nonlinear dynamic of picosecond pulse propagation in atmospheric air-filled hollow core fibers," Opt. Express **26**, 8866-8882 (2018).
4. F. Yu, W. J. Wadsworth, and J. C. Knight, "Low loss silica hollow core fibers for 3–4 μm spectral region," Opt. Express **20**, 11153-11158 (2012).
5. F. Yu, M. Cann, A. Brunton, W. Wadsworth, and J. Knight, "Single-mode solarization-free hollow-core fiber for ultraviolet pulse delivery," Optics express **26**, 10879-10887 (2018).
6. W. Jin, H. L. Ho, Y. C. Cao, J. Ju, and L. F. Qi, "Gas detection with micro- and nano-engineered optical fibers," Optical Fiber Technology **19**, 741-759 (2013).
7. J. R. Hayes, F. Poletti, M. S. Abokhamis, N. V. Wheeler, N. K. Baddela, and D. J. Richardson, "Anti-resonant hexagram hollow core fibers," Opt. Express **23**, 1289-1299 (2015).
8. G. T. Jasion, J. S. Shrimpton, Y. Chen, T. Bradley, D. J. Richardson, and F. Poletti, "Microstructure element method (msem): Viscous flow model for the virtual draw of microstructured optical fibers," Opt. Express **23**, 312-329 (2015).
9. M. J. Chen, Y. M. Stokes, P. Buchak, D. G. Crowdy, H. T. C. Foo, A. Dowler, and H. Ebendorff-Heidepriem, "Drawing tubular fibres: Experiments versus mathematical modelling," Opt. Mat. Express **6**, 166-180 (2016).
10. S. C. Xue, R. I. Tanner, G. W. Barton, R. Lwin, M. C. J. Large, and L. Poladian, "Fabrication of microstructured optical fibers-part ii: Numerical modeling of steady-state draw process," J. Lightwave Technol. **23**, 2255-2266 (2005).
11. A. D. Fitt, K. Furusawa, T. M. Monro, C. P. Please, and D. J. Richardson, "The mathematical modelling of capillary drawing for holey fibre manufacture," J. Eng. Math. **43**, 201-227 (2002).
12. A. Fasano, H. K. Rasmussen, and J. M. R. Marín, "3d viscoelastic finite element modelling of polymer flow in the fiber drawing process for microstructured polymer optical fiber fabrication," in *The 24th International Conference on Plastic Optical Fibers* (2015).
13. S. S. Chakravarthy, and W. K. Chiu, "Boundary integral method for the evolution of slender viscous fibres containing holes in the cross-section," J. Fluid Mech. **621**, 155-182 (2009).
14. Y. M. Stokes, P. Buchak, D. G. Crowdy, and H. Ebendorff-Heidepriem, "Drawing of micro-structured fibres: Circular and non-circular tubes," J. Fluid Mech. **755**, 176-203 (2014).
15. H. Tronnolone, *Extensional and surface-tension-driven fluid flows in microstructured optical fibre fabrication* (University of Adelaide, 2016).
16. A. N. Kolyadin, A. F. Kosolapov, A. D. Pryamikov, A. S. Biriukov, V. G. Plotnichenko, and E. M. Dianov, "Light transmission in negative curvature hollow core fiber in extremely high material loss region," Opt. Express **21**, 9514-9519 (2013).
17. D. J. Richardson, Y. Chen, N. Wheeler, J. Hayes, T. Bradley, Z. Liu, S. R. Sandoghchi, G. Jasion, E. Numkam Fokoua, D. Gray, R. Slavík, Y. Jung, N. Wong, F. Poletti, and M. Petrovich, "Photonic bandgap fibres for low-latency data transmission," (2015).
18. N. V. Wheeler, T. D. Bradley, J. R. Hayes, M. A. Gouveia, S. Liang, Y. Chen, S. R. Sandoghchi, S. M. A. Mousavi, F. Poletti, and M. N. Petrovich, "Low-loss kagome hollow-core fibers operating from the near-to the mid-ir," Opt. Lett. **42**, 2571-2574 (2017).
19. A. F. Kosolapov, G. K. Alagashev, A. N. Kolyadin, A. D. Pryamikov, A. S. Biryukov, I. A. Bufetov, and E. M. Dianov, "Hollow-core revolver fibre with a double-capillary reflective cladding," Quantum Electronics **46**, 267 (2016).
20. J. R. Hayes, S. R. Sandoghchi, T. D. Bradley, Z. Liu, R. Slavík, M. A. Gouveia, N. V. Wheeler, G. Jasion, Y. Chen, and E. N. Fokoua, "Antiresonant hollow core fiber with an octave spanning bandwidth for short haul data communications," J. Lightwave Technol. **35**, 437-442 (2017).
21. M. Chafer, F. Delahaye, F. Amrani, B. Debord, F. Gérôme, and F. Benabid, "1 km long hc-pcf with losses at the fundamental rayleigh scattering limit in the green wavelength range," in *CLEO*(Optical Society of America, USA, 2018), pp. SF1K-3.
22. W. Belardi, and J. C. Knight, "Hollow antiresonant fibers with reduced attenuation," Opt. Lett. **39**, 1853-1856 (2014).
23. F. Poletti, "Nested antiresonant nodeless hollow core fiber," Optics Express **22**, 23807-23828 (2014).
24. S. F. Gao, Y. Y. Wang, W. Ding, D. L. Jiang, S. Gu, X. Zhang, and P. Wang, "Hollow-core conjoined-tube negative-curvature fibre with ultralow loss," Nature communications **9**, 2828 (2018).
25. T. D. Bradley, J. R. Hayes, Y. Chen, G. T. Jasion, S. R. Sandoghchi, R. Slavik, E. N. Fokoua, S. Bawn, H. Sakr, I. A. Davidson, A. Taranta, J. P. Thomas, M. N. Petrovich, D. J. Richardson, and F. Poletti, "Record low-loss 1.3db/km data transmitting antiresonant hollow core fibre," in *2018 European Conference on Optical Communication (ECOC)*(Rome, Italy, 2018), pp. 1-3.

26. C. Wei, R. Joseph Weiblen, C. R. Menyuk, and J. Hu, "Negative curvature fibers," Adv. Opt. Photon. **9**, 504-561 (2017).
27. W. Belardi, and J. C. Knight, "Hollow antiresonant fibers with low bending loss," Opt. Express **22**, 10091-10096 (2014).
28. I. A. Bufetov, A. F. Kosolapov, A. D. Pryamikov, A. V. Gladyshev, A. N. Kolyadin, A. A. Krylov, Y. P. Yatsenko, and A. S. Biriukov, "Revolver hollow core optical fibers," Fibers **6**, 39 (2018).
29. S. C. Xue, L. Poladian, G. W. Barton, and M. C. J. Large, "Radiative heat transfer in preforms for microstructured optical fibres," Int. J. Heat Mass Tran. **50**, 1569-1576 (2007).
30. S. R. Sandoghchi, D. Gray, Y. Chen, N. Wheeler, T. Bradley, J. Hayes, E. Numkam Fokoua, G. Jasion, S. M. Abokhamis Mousavi, M. Petrovich, and F. Poletti, "High dynamic range technique for discrete and distributed scattering loss measurement in microstructured optical fibres," (2015).
31. Y. Chen, and T. A. Birks, "Predicting hole sizes after fibre drawing without knowing the viscosity," Opt. Mat. Express **3**, 346-356 (2013).
32. G. Urbain, Y. Bottinga, and P. Richet, "Viscosity of liquid silica, silicates and alumino-silicates," Geochim. Cosmochim. Acta **46**, 1061-1072 (1982).
33. R. H. Doremus, "Viscosity of silica," J. Appl. Phys. **92**, 7619-7629 (2002).
34. Heraeus, "Heraeus quarzglas: Thermal properties, fused silica," http://heraeus-quarzglas.com/en/quarzglas/thermalproperties/Thermal_properties.aspx, Accessed 05/12, 2018.
35. H. Schonhorn, H. Vazirani, and H. Frisch, "Relationship between fiber tension and drawing velocity and their influence on the ultimate strength of laser-drawn silica fibers," J. Appl. Phys. **49**, 3703-3706 (1978).
36. Y. Chen, Z. Liu, S. R. Sandoghchi, G. T. Jasion, T. D. Bradley, E. Numkam Fokoua, J. R. Hayes, N. V. Wheeler, D. R. Gray, B. J. Mangan, R. Slavík, F. Poletti, M. N. Petrovich, and D. J. Richardson, "Multi-kilometer long, longitudinally uniform hollow core photonic bandgap fibers for broadband low latency data transmission," J. Lightwave Technol. **34**, 104-113 (2016).
37. M. S. Habib, O. Bang, and M. Bache, "Low-loss hollow-core silica fibers with adjacent nested anti-resonant tubes," Opt. Express **23**, 17394-17406 (2015).
38. D. Bird, "Attenuation of model hollow-core, anti-resonant fibres," Opt. Express **25**, 23215-23237 (2017).
39. M. I. Hasan, N. Akhmediev, and W. Chang, "Positive and negative curvatures nested in an antiresonant hollow-core fiber," Opt. Lett. **42**, 703-706 (2017).
40. F. Meng, B. Liu, Y. Li, C. Wang, and M. Hu, "Low loss hollow-core antiresonant fiber with nested elliptical cladding elements," IEEE Photonics Journal **9**, 1-11 (2017).
41. M. S. Habib, J. E. Antonio-Lopez, C. Markos, A. Schülzgen, and R. Amezcua-Correa, "Single-mode, low loss hollow-core anti-resonant fiber designs," Opt. Express **27**, 3824-3836 (2019).
42. Y. Zhu, M. Chen, and Y. Liu, "Nested low-loss hollow core fiber," IEEE Journal of Selected Topics in Quantum Electronics, 1-1 (2019).
43. G. T. Jasion, D. J. Richardson, and F. Poletti, "Novel antiresonant hollow core fiber design with ultralow leakage loss using transverse power flow analysis," in *Optical Fiber Communication Conference (OFC)*(Optical Society of America, San Diego, California, 2019), p. Th3E.2.